



**HAL**  
open science

# Three-dimensional hydromechanical modeling of internal erosion in dike-on-foundation

Jie Yang, Zhen-Yu Yin, Farid Laouafa, Pierre-Yves Hicher

## ► To cite this version:

Jie Yang, Zhen-Yu Yin, Farid Laouafa, Pierre-Yves Hicher. Three-dimensional hydromechanical modeling of internal erosion in dike-on-foundation. *International Journal for Numerical and Analytical Methods in Geomechanics*, 2020, 44 (8), pp.1200-1218. 10.1002/nag.3057 . ineris-03318125

**HAL Id: ineris-03318125**

**<https://ineris.hal.science/ineris-03318125>**

Submitted on 6 Apr 2022

**HAL** is a multi-disciplinary open access archive for the deposit and dissemination of scientific research documents, whether they are published or not. The documents may come from teaching and research institutions in France or abroad, or from public or private research centers.

L'archive ouverte pluridisciplinaire **HAL**, est destinée au dépôt et à la diffusion de documents scientifiques de niveau recherche, publiés ou non, émanant des établissements d'enseignement et de recherche français ou étrangers, des laboratoires publics ou privés.

# Three-dimensional hydro-mechanical modelling of internal erosion in dike-on-foundation

Jie YANG<sup>1,2,3</sup>, Zhen-Yu YIN<sup>1,\*</sup>, Farid LAOUAFA<sup>2</sup>, Pierre-Yves HICHER<sup>3</sup>

## Affiliations:

<sup>1</sup> Department of Civil and Environmental Engineering, The Hong Kong Polytechnic University, Hung Hom, Kowloon, Hong Kong, China

<sup>2</sup> French National Institute for Industrial Environment and Risks (INERIS), Verneuil-en-Halatte, France

<sup>3</sup> Research Institute of Civil Engineering and Mechanics (GeM), UMR CNRS 6183, Ecole Centrale de Nantes, France

\* Corresponding authors: Dr. Zhen-Yu YIN, Tel: +852 3400 8470; Fax: +852 2334 6389; Email: [zhenyu.yin@polyu.edu.hk](mailto:zhenyu.yin@polyu.edu.hk); [zhenyu.yin@gmail.com](mailto:zhenyu.yin@gmail.com)

**Summary:** Currently, numerical studies at the real scale of an entire engineering structure considering internal erosion are still rare.

This paper presents a 3D numerical simulation of the effects of internal erosion within a linear dike located on a foundation. A 2D finite element code has been extended to 3D in order to analyze the impact of internal erosion under more realistic hydro-mechanical conditions. The saturated soil has been considered as a mixture of four interacting constituents: soil skeleton, erodible fines, fluidized fine particles, and fluid. The detachment and transport of the fine particles have been modeled with a mass exchange model between the solid and the fluid phases. An elasto-plastic constitutive model for sand-silt mixtures has been developed to monitor the effect of the evolution of both the porosity and the fines content induced by internal erosion upon the behavior of the soil skeleton. An unsaturated flow condition has been implemented into this coupled hydro-mechanical model to describe more accurately the seepage within the dike and the foundation. A stabilized finite element method was used to eliminate spurious numerical oscillations in solving the convection-dominated transport of fluidized particles. This numerical tool was then applied to a specific dike-on-foundation case subjected to internal erosion induced by a leakage located at the bottom of the foundation. Different failure modes were observed and analyzed for different boundary conditions, including the significant influence of the leakage cavity size and the elevation of the water level at the upstream and downstream sides of the dike.

**Keywords:** granular media; dike; internal erosion; critical state; fines content; stabilized finite element method

## 1. Introduction

Internal erosion occurs when fine particles are plucked off by hydraulic forces and transported through a coarse porous matrix. The known causes are either a concentration of leak erosion, backward erosion, soil contact erosion, or suffusion<sup>1-3</sup>. This paper focuses on suffusion, which corresponds to the detachment and migration of fine particles within the voids (pores) of coarse particles by means of seepage flow. Due to the loss of a part of the solid phase, the mechanical properties of the soil are progressively modified and degraded, and with time, earthen structures may be subjected to risk of failure<sup>2, 4-7</sup>. Foster et al.<sup>8</sup> showed that nearly 46% of the damage of 128 embankment dams could be attributed to internal erosion. Moreover, sinkholes and cavities triggered by internal erosion are frequently observed within dams and dikes<sup>9, 10</sup>. Internal erosion can also trigger slope failures and generate significant landslides<sup>11, 12</sup>.

Laboratory experimental tests<sup>13-17</sup> and numerical analyses<sup>18-24</sup> at the scale of the representative elementary volume have undoubtedly played an important role in understanding the physical mechanisms behind internal erosion phenomena. However, these studies have not provided a clear understanding of where and when seepage flow could trigger internal instability in a granular soil mixture at larger space scales for real boundary value problems. Several physical tests have been carried out for this purpose<sup>12, 25, 26</sup>. However, few numerical studies at the scale of an engineering structure are available in the literature<sup>18, 19, 21, 27, 28</sup>. In the available studies, the mechanical responses of an eroded soil were often bypassed or simplified by using an elastic model with induced damage parameters. Yang et al.<sup>29</sup> proposed a coupled hydro-mechanical approach based on porous continuous medium theory to assess how internal erosion impacts the safety of earthen structures. They developed an elasto-plastic constitutive model for sand-silt mixtures to monitor the effect of the evolution of both the porosity and the fines content induced by internal erosion upon the behavior of the soil skeleton. This model was then applied to analyse internal erosion within a fully saturated dike under plane strain condition. However, a three-dimensional (3D) condition has long been thought to be a significant factor in the internal erosion process. Under 3D conditions, the constraint of the surrounding soil may limit or delay the development of the soil deformation, which may in turn introduce a more 'local' failure-collapse mode (*i.e.*, a sinkhole) instead of a landslide-type instability.

The aim of this study is to simulate the 3D mechanical consequences of internal erosion within a linear dike on a foundation under more general and realistic conditions. First, the unsaturated flow condition was implemented into the coupled hydro-mechanical model of Yang et al.<sup>29</sup> in order to describe more accurately the seepage within the dike and foundation due to the difference in water pressure at the upstream and downstream sides of the dike-on-foundation. Afterwards, the enhanced model was implemented into a 3D finite element code using a stabilized finite element method. Then it was applied to simulate the effect of internal erosion induced by a seepage flow within a dike, and a leakage at the bottom of the foundation due to the presence of a cavity. The influence of the leakage cavity size and the elevation of the water level at the upstream and downstream sides of the dike-on-foundation were thus analysed.

## 2. Coupled hydro-mechanical model

### 2.1. Mass balances and transported particles

According to Vardoulakis et al.<sup>18</sup> and Schaufler et al.<sup>30</sup>, it is possible to consider a saturated porous medium as a material system composed of 4 constituents in 2 phases: the stable fabric of the solid skeleton, erodible fines, fluidized particles and pure fluid. The fines can behave either as a fluid-like (described as fluidized particles) or as a solid-like (described as erodible fines) material. The hydraulic process of suffusion can be described by a system of non-linear partial differential equations deduced from the mass balance of the mixture system (More details can be found in<sup>29</sup>):

$$\operatorname{div}(\mathbf{q}_w) + \operatorname{div}(\mathbf{v}_s) = 0 \quad \dots\dots\dots (1)$$

$$-\frac{\partial \phi}{\partial t} + \operatorname{div}(\mathbf{v}_s) - \operatorname{div}(\phi \mathbf{v}_s) = \hat{n} \quad \dots\dots\dots (2)$$

$$\frac{\partial (f_c)}{\partial t} - \frac{\partial (f_c \phi)}{\partial t} + \operatorname{div}(f_c \mathbf{v}_s) - \operatorname{div}(f_c \phi \mathbf{v}_s) = \hat{n} \quad \dots\dots\dots (3)$$

$$\frac{\partial (c \phi)}{\partial t} + \operatorname{div}(c \mathbf{q}_w) + \frac{\partial (c \phi \mathbf{v}_s)}{\partial t} = -\hat{n} \quad \dots\dots\dots (4)$$

where  $\phi(x,t)$ ,  $f_c(x,t)$  and  $c(x,t)$  are the porosity, the amount of erodible fines and the concentration of the fluidized particles, respectively;  $\hat{n}$  is the source term describing the exchange between the erodible fines and the fluidized particles;  $\mathbf{v}_s$  is the velocity of the soil

skeleton and  $\mathbf{q}_w(x, t)$  is the total discharge of the pore fluid assumed to be governed by Darcy's law:

$$\mathbf{q}_w = -\frac{k}{\eta_k \bar{\rho}} \mathbf{grad}(p_w) \dots\dots\dots (5)$$

with the intrinsic permeability of the medium  $k$  and the density of the mixture  $\bar{\rho}(c)$  defined as:

$$k = k_0 \frac{\phi^3}{(1-\phi)^2} \dots\dots\dots (6)$$

$$\bar{\rho} = c\rho_s + (1-c)\rho_f \dots\dots\dots (7)$$

where  $\eta_k$  is the kinematic viscosity of the fluid,  $p_w$  is the pore fluid pressure,  $\rho_s$  and  $\rho_f$  are the density of the solid and the fluid, respectively, and  $k_0$  is the permeability parameter of Kozeny-Carman relationship <sup>31</sup>.

## 2.2. Erosion law

The variable  $\hat{n}$  in Eqs. (2)-(4) is the volumetric mass exchange at any point in time, which determines the rate of erosion. It should be defined by an appropriate erosion law. Since the proposed numerical approach is modular and independent of the erosion law, it is possible to choose the most appropriate expression of the erosion law for different cases. Due to the lack of experimental data, the present paper is mainly a theoretical study. Its focus is not upon a comparison with a real case and it does not discuss the choice of the erosion law. A simple erosion law <sup>28</sup> has therefore been adopted as follow:

$$\hat{n} = -\lambda_e f_c |\mathbf{q}_w| \dots\dots\dots (8)$$

where  $\lambda_e$  is a material parameter, experimentally determined. Furthermore, in the following analyses, a residual fines content has been artificially introduced for the sake of simplicity.

## 2.3. Unsaturated flow in dike-on-foundation

For isotropic partially saturated porous continua, the classical expression for the Cauchy effective stress tensor  $\boldsymbol{\sigma}'$  consistent with continuum principles of thermodynamics can be expressed as follows <sup>32</sup>:

$$\boldsymbol{\sigma}' = \boldsymbol{\sigma} + B\bar{p}\mathbf{I} \dots\dots\dots (9)$$

$$\bar{p} = s_w p_w + s_a p_a \dots\dots\dots (10)$$

where  $\boldsymbol{\sigma}$  is the total Cauchy stress tensor,  $B$  is the Biot coefficient,  $\mathbf{I}$  is the second-order identity tensor and  $\bar{p}$  is the mean pore pressure;  $p_w$  and  $p_a$  are the pore water and pore air pressures, and  $s_w$  and  $s_a$  are the degrees of water saturation and air saturation, respectively.

The tensile stresses are considered positive, which explains the sign in Eq. (9). We consider in the following a Biot coefficient  $B$  equal to one<sup>33</sup>. In a transient and quasi-static analysis, the model can be simplified by assuming that the air pressure is constant throughout the domain and is small enough so that its value can be disregarded. This simplification reduces the effective stress expression to:

$$\boldsymbol{\sigma}' = \boldsymbol{\sigma} - s_w p_c \mathbf{I}, \dots\dots\dots (11)$$

with  $p_c = -p_w$

Therefore, the medium is fully saturated for  $p_w > 0$ ; negative values of  $p_w$  represent the capillary effects. For  $p_w < 0$ , it is known that at a given value of the capillary pressure,  $p_c (= -p_w)$ , the saturation condition lies within certain limits<sup>34,35</sup>. In this study, the empirical soil-water characteristic curve (SWCC) proposed by van Genuchten<sup>34</sup>, which has been proved to be suitable for silty sand<sup>34</sup>, was adopted to explicitly determine the degree of water saturation for a given capillary pressure.

In the van Genuchten model, the SWCC is expressed as follows<sup>34</sup>:

$$s_w = (s_{w,s} - s_{w,r}) s_{w,e} + s_{w,r}$$

$$s_{w,e} = \left[ 1 + (\alpha_{vg} p_c)^{n_{vg}} \right]^{-m_{vg}} \dots\dots\dots (12)$$

where  $s_{w,e}$  is the effective degree of water saturation;  $s_{w,r}$  is the residual (minimum) degree of water saturation;  $s_{w,s}$  is the maximum degree of water saturation ( $s_{w,s} = 1.0$ ), and  $\alpha_{vg}$ ,  $n_{vg}$  and  $m_{vg}$  are the material parameters of the van Genuchten model. For  $p_c < 0$  (saturated medium), the effective degree of saturation  $s_{w,e}$  was set to be 1.0.

The water permeability coefficients within the van Genuchten model were assumed to be dependent on effective water saturation as:

$$k = k_s (s_{w,e})^{\xi_{vg}} \left[ 1 - \left\{ 1 - (s_{w,e})^{1/m_{vg}} \right\}^{m_{vg}} \right]^2 \dots\dots\dots (13)$$

where  $k_s$  is the saturated (maximum) coefficient of water permeability and  $\xi_{vg}$  is a material parameter.

Therefore, the unsaturated flow could be introduced into the hydro-mechanical model for internal erosion by combining Eqs. (11)-(13) with Eqs. (1)-(4). A critical state based constitutive model was adopted to determine the Cauchy effective stress. This model has the capacity to consider the impact of the change of porosity and fines content upon the mechanical behavior of the soil during the erosion process, as described below. Note that in this study, the foundation soil was considered as a sandy soil with coarse grains, and thus, the above modification to the effective stresses was suitable when applied directly to the saturated sand model.

**2.4. Critical state based soil model considering fines effect**

To assess the mechanical response to the loss of fines content induced by internal erosion in an earthen structure, it was decided to adopt a non-associated elastoplastic constitutive model for sand-silt mixture for the solid skeleton <sup>36</sup>. This model was extended from the basic SIMSAND model <sup>37, 38</sup> under the framework of the critical state concept and elastoplasticity theory (summarized in Appendix) by defining the position of the critical state line as a function of the fines content in order to unify the mechanical behavior of a sand-silt mixture from silt to sand or sand to silt (see (14) and (15)). Therefore, this model takes into account the influence of the porosity and the fines content evolution on the mechanical behavior of the soil during the erosion process. It should be noted that for sandy soils, only the shear yield surface is needed.

A non-linear expression of the critical state line is adopted here, and has the following expression:

$$e_c = e_{cr0} - \lambda \left( \frac{p'}{p_{at}} \right)^{\xi} \dots\dots\dots (14)$$

where  $e_{cr0}$  is the reference critical void ratio corresponding to the void ratio  $e$  at the mean effective stress  $p'=0$  .  $e_{cr0}$  determines the position of the CSL in the  $e-p'$  plane.

$p_{at} = 101.325 \text{ kPa}$  is the atmospheric pressure.  $\lambda$  and  $\xi$  are material constants controlling the non-linearity of the critical state line.

Given the evolution of the fines content during internal erosion, the constitutive model needs to take into account such internal soil mass evolution. Yin et al. <sup>36, 39</sup> considered  $e_{cr0}$  as a function of the fines content in order to unify the mechanical behavior of a sand-silt mixture for different fines contents:

$$e_{cr0} = \left[ e_{hc,cr0} (1 - f_c) + a f_c \right] \frac{1 - \tanh[\zeta (f_c - f_{th})]}{2} + e_{hf,cr0} \left( f_c + \frac{1 - f_c}{(R_d)^m} \right) \frac{1 + \tanh[\zeta (f_c - f_{th})]}{2} \dots\dots (15)$$

The function was mathematically structured based on the hyperbolic tangent function  $\tanh x = (e^{2x} - 1) / (e^{2x} + 1)$  to ensure a smooth transition between a silty sand and a sandy silt.  $e_{hc,cr0}$  and  $e_{hf,cr0}$  are the reference critical void ratios for pure sand and pure silt, respectively.  $a$ ,  $\zeta$ ,  $R_d$ ,  $m$  and  $f_{th}$  are material constants. More details can be found in Yin et al. <sup>36, 39</sup>.

A finite difference code was developed to investigate the validity of the proposed model <sup>40-42</sup>. The comparison between experimental results and simulations demonstrated that, with an appropriate erosion law and well calibrated model parameters, the numerical model was able to reproduce with success the initiation and development of internal erosion.

### 3. Finite element approach

#### 3.1. Standard Galerkin-weighted residual method

The following governing equations were obtained by combining the balance and constitutive equations in order to formulate the Initial Boundary Value Problem (IBVP) of internal erosion:

$$\sigma_{ij,j} - w_j = 0 \dots\dots\dots (16)$$

$$\text{div}(v_s) + \text{div}(q_w) = 0 \dots\dots\dots (17)$$

$$-\frac{\partial(\phi)}{\partial t} + \text{div}(v_s) - \text{div}(\phi v_s) + \lambda_e f_c |q_w| = 0 \dots\dots\dots (18)$$

$$\frac{\partial(c\phi)}{\partial t} + \text{div}(c q_w) + \text{div}(c \phi v_s) - \lambda_e f_c |q_w| = 0 \dots\dots\dots (19)$$

$$q_w + \frac{k}{\eta_k \bar{\rho}} \text{grad}(p_w) = 0 \dots\dots\dots (20)$$

where  $w_i$  denotes the body force per unit volume. Together with Eqs. (6)-(15), a system of 5 equations with 5 unknowns  $(\mathbf{u}, p_w, \phi, c, \mathbf{q}_w)$  was obtained: the soil skeleton displacement  $(\mathbf{u}(\mathbf{x}, t))$ , the pore pressure  $(p_w(\mathbf{x}, t))$ , the porosity  $(\phi(\mathbf{x}, t))$ , the concentration of fluidized particles  $(c(\mathbf{x}, t))$  and the flow rate  $q_w(\mathbf{x}, t)$ . For the sake of legibility, the time  $t$  and the space  $\mathbf{x}$  variables have been omitted in the equations.

This coupled mechanical-erosion process is a non-linear transient problem. Weak forms of the governing partial differential equations were implemented into the finite element code ABAQUS<sup>43</sup>. ABAQUS<sup>43</sup> provides a user subroutine option (UEL) that allows users to define a new type of element with user's defined governing equations and degrees of freedom (DOFs). The subroutine makes it possible to use advantageously the powerful pre- and post-processing and highly efficient matrix solver of ABAQUS. The global calculate flow of ABAQUS with the call of UEL subroutine is shown in Figure 1 where the part of "from Call UEL to update RHS" was developed in this study. In general, Abaqus/UEL solves the overall system of non-linear equations by Newton's method:

$$\mathbf{AMATRIX} \cdot \mathbf{d}_N = \mathbf{RHS} \dots\dots\dots (21)$$

where **AMATRIX** and **RHS** are the Jacobian matrix and the residual nodal fluxes or forces needed to be defined corresponding to Eqs. (16)-(20);  $\mathbf{d}_N$  is the nodal vector of the DOFs  $(u_x, u_y, u_z, p_w, \phi, c, q_{wx}, q_{wy}, q_{wz})$ . A new isoparametric brick element with 9 DOFs has been developed and implemented into ABAQUS via the UEL subroutine. The detailed vector of residual and the Jacobian matrix can be found in Yang et al.<sup>29</sup>

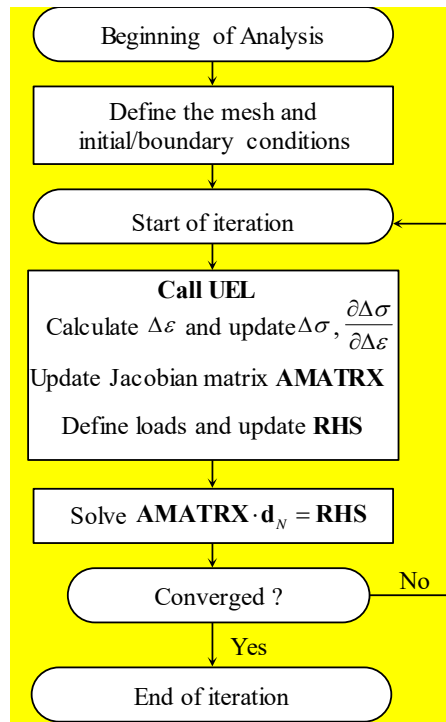


**Figure 1. Global calculate flow of ABAQUS with the call of UEL subroutine**

### 3.2. Stabilized finite element method

Several problems were noted in the treatment of the convection (advective) dominated flows (Eq. (19)). Numerical oscillation occurred when the standard Galerkin method was applied to convection dominated flows, affecting the computation accuracy and efficiency<sup>44, 45</sup>. The non-linear convection terms render the governing differential equations non-self-adjoint<sup>46</sup>. The matrix associated with the convective term is non-symmetric. As a result, the “best approximation”<sup>47</sup> property is lost, resulting in numerical oscillations.

In practice, the oscillations become more significant as the Péclet number increases, which is a function of the properties of the porous medium governing diffusion and velocity of the fluid, as well as the finite element size<sup>48-50</sup>. Solutions are often corrupted by spurious oscillations when a downstream boundary condition forces a rapid change in the solution. One way to eliminate such numerical oscillations is to refine the mesh, such that convection no longer dominates at an element level<sup>44</sup>. However, the prohibitive computational cost in 3D condition becomes an obstacle whenever real soil structures such as embankment dams are studied. This has provided motivation for an alternative to the Galerkin formulation that precludes spurious oscillations regardless of mesh refinement.

In the last decades, considerable effort has been made towards developing a stabilized finite element method to improve the numerical solutions of the heat or solute transport problems<sup>44</sup>,

51-59. The present paper does not focus upon a comparison of different algorithms. The Petrov-Galerkin weighted residual method proposed by Yu and Heinrich<sup>51,52</sup> was employed for solving Eq. (19). The method involves perturbed weighting functions in the weighted residual formulations that depend on two parameters ( $\alpha$ ,  $\beta$ ) calculated according to a local analysis. The perturbations to the weighting functions can be interpreted as an added local anisotropic balancing diffusion and an added dispersion in the direction of the convective motion. The integration of the weak form of Eq. (19) from time  $t$  to  $t + \Delta t$  provides an average equilibrium statement for the increment, which gives:

$$\begin{aligned}
& \frac{1}{\Delta t} \int \phi \left( \mathbf{N}^N + \alpha \frac{h}{2} \frac{\mathbf{v}}{|\mathbf{v}|} \frac{\partial \mathbf{N}^N}{\partial \mathbf{x}} \right) \mathbf{N}^M dV (c^{M,t+\Delta t} - c^{M,t}) \\
& + \frac{1}{2} \int \left( \mathbf{N}^N + \alpha \frac{h}{2} \frac{\mathbf{v}}{|\mathbf{v}|} \frac{\partial \mathbf{N}^N}{\partial \mathbf{x}} \right) \mathbf{v} \frac{\partial \mathbf{N}^M}{\partial \mathbf{x}} dV (c^{M,t+\Delta t} + c^{M,t}) \\
& - \frac{\beta h}{4} \int \frac{\mathbf{v}}{|\mathbf{v}|} \frac{\partial \mathbf{N}^N}{\partial \mathbf{x}} \mathbf{v} \frac{\partial \mathbf{N}^M}{\partial \mathbf{x}} dV (c^{M,t+\Delta t} - c^{M,t}) \\
& + \int \left( \mathbf{N}^N + \alpha \frac{h}{2} \frac{\mathbf{v}}{|\mathbf{v}|} \frac{\partial \mathbf{N}^N}{\partial \mathbf{x}} \right) \left( \hat{n} + c \frac{\Delta \phi}{\Delta t} \right) dV = 0
\end{aligned} \tag{22}$$

where  $\mathbf{N}^N$  are shape functions,  $\mathbf{v}$  is the average fluid velocity over the element;  $|\mathbf{v}|$  is its Euclidean norm;  $h$  is a characteristic element length measure, defined as:

$$h = \sum_{\alpha} |h_{\alpha}| \quad \text{and} \quad h_{\alpha} = \mathbf{h}_{\alpha} \cdot \frac{\mathbf{v}}{|\mathbf{v}|} \tag{23}$$

where  $\mathbf{h}_{\alpha}$  is the  $\alpha$  isoparametric line across the element, passing through its centroid.  $h_{\alpha}$  is the projection of  $\mathbf{h}_{\alpha}$  in the direction of the fluid velocity vector at the element centroid.

In Eq.(22),  $\alpha$  and  $\beta$  are control parameters. The  $\alpha$  term in the weighting function was introduced to eliminate artificial diffusion of the solution, while the  $\beta$  term was introduced to avoid numerical dispersion, given as<sup>51,52</sup>:

$$\alpha = \coth \frac{\gamma}{2} - \frac{2}{\gamma} \quad \text{and} \quad \beta = \frac{C}{3} - \frac{2}{\gamma} \frac{\alpha}{C} \tag{24}$$

$$\gamma = |\mathbf{v}| h \frac{\rho c}{k} \quad \text{and} \quad C = |\mathbf{v}| \frac{\Delta t}{h} \tag{25}$$

where  $\gamma$  is the local Péclet number in an element and  $C$  is the local Courant number.

It should be noted that the deformation terms have been omitted from the equilibrium equation (22) for the sake of simplicity, which assumes that the deformation of the specific domain will not change the concentration of the fluidized fine particles.

## **4. Three-dimensional modeling of internal erosion within a dike**

### **4.1. Description of the problem**

The characteristics of the studied configuration are presented in Figure 2 according to the case study of the dike of Val d'Orléans <sup>60</sup>. The dike was built on sandy-silt alluvium formation over limestone. The upstream face of the dike-on-foundation (Face  $S_1$  in Figure 2) is exposed to the water within the river behind the dike. Likewise, the downstream face of the dike-on-foundation (Face  $S_4$  in Figure 2) is exposed to the atmosphere. If the soil is partially saturated, the phreatic surface in the dike and foundation (Face  $S_2$  in Figure 2) corresponds to the locus of the points at which the pore fluid pressure,  $p_w$ , is equal to zero. Above this surface, the pore fluid pressure is negative, which represents the capillary tension that causes the fluid to rise against gravitational forces, creating a capillary zone. The saturation associated to specific values of the capillary pressure for the absorption of the fluid by the porous medium is a physical property of the material and has been defined by the van Genuchten model. The bottom of the alluvium layer (Face  $S_3$  in Figure 2) was assumed to rest on an impermeable limestone layer. The seepage due to the water pressure gradient at the upstream and downstream faces of the dike-on-foundation could lead to the detachment of fine particles that will move from the upstream to the downstream side, eventually leading to the degradation of the dike. Furthermore, in the case of the Val d'Orléans dike, it has been reported that karst collapses underneath the foundation might lead to a leakage cavity through which underground water and fine particles could flow out. Internal erosion could occur due to local hydraulic gradients in the vicinity of the cavity. The computations aimed to show how internal erosion may weaken the foundation and the dike under different boundary conditions.

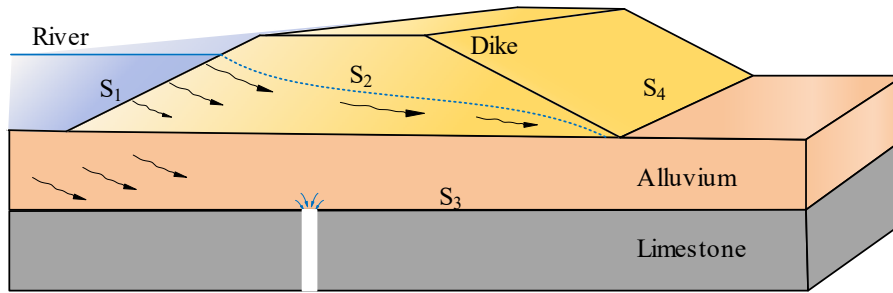


Figure 2 Scheme of the dike-on-foundation near Orléans (France) with a cavity located at the bottom.

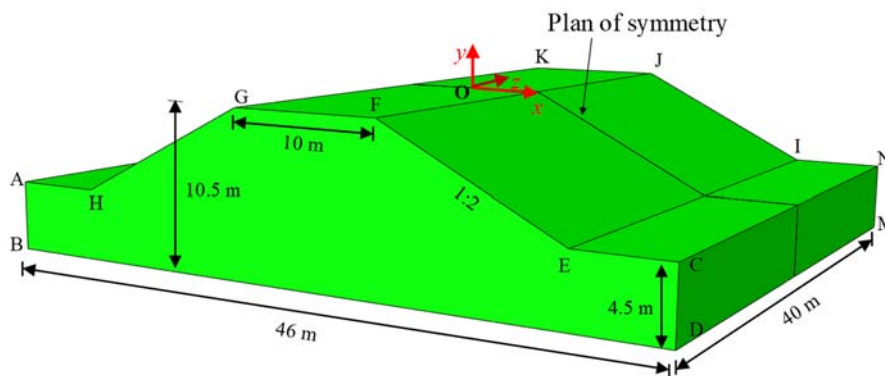


Figure 3 Schematic configuration of the dike and mesh of the numerical model

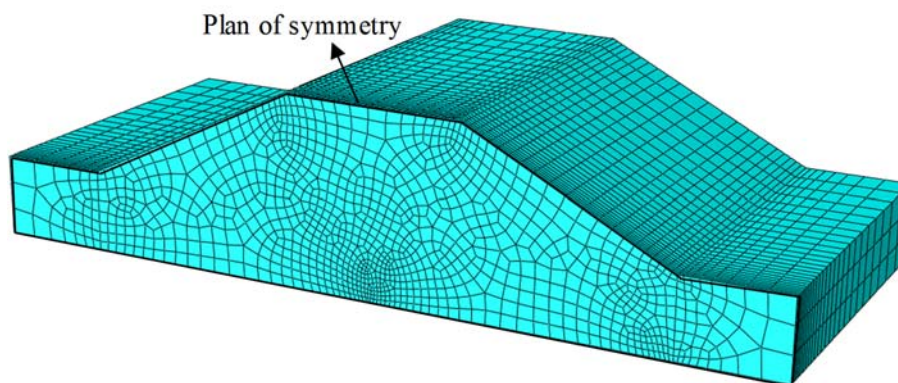


Figure 4 Mesh of numerical model (1/2 model due to symmetry)

The dimensions of the analyzed model are shown in Figure 3. The problem was analysed under the assumption of a symmetric condition; thus, only half of the specific domain was modelled with 34346 second order brick elements, shown in Figure 4. Two cases with different hydraulic boundary conditions were simulated. In both cases, the water level at the upstream face was located at the top of the dike (*i.e.* 10.5 m), representing an extreme configuration of the flooding condition. The water level at the downstream face was supposed to be located at the bottom of the alluvium layer, below the toe of the dike, as shown in Figure 5. The phreatic surface was calculated accordingly. Furthermore, in case 2, a leakage cavity of 0.2 m in diameter created by a karst collapse underneath the alluvium layer was

assumed to exist at the bottom of the symmetry plane of the model, where the water pressure was assumed to be zero.

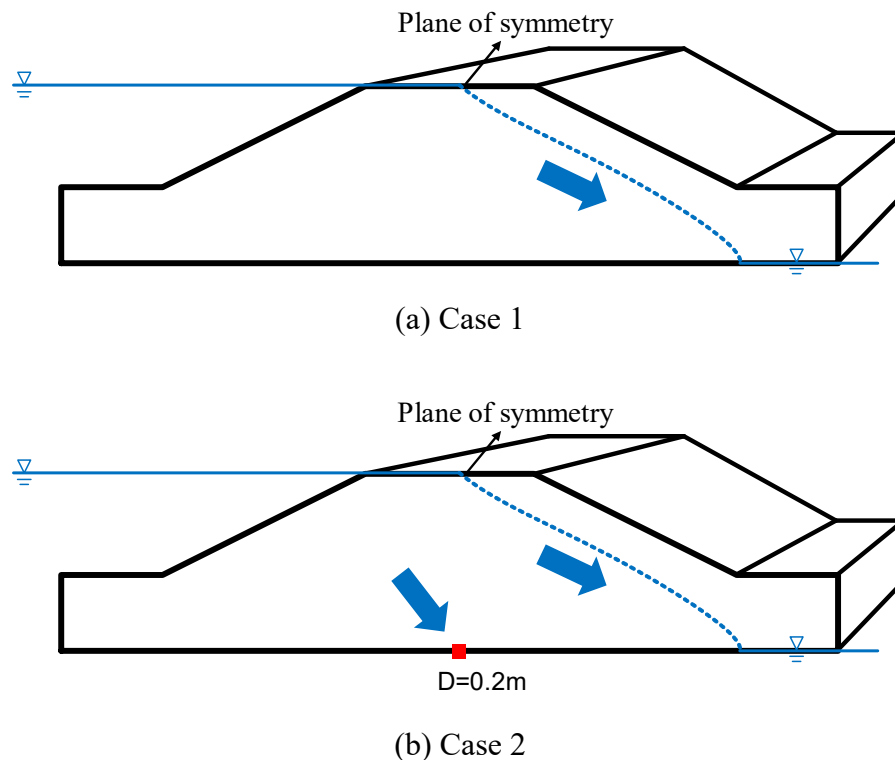


Figure 5 Boundary hydraulic conditions for: (a) Case1-without the cavity; and (b) Case 2-with the cavity (diameter  $D=0.2\text{ m}$ )

The boundary conditions were taken as symmetry plane (rollers) on the left and right boundary surfaces of the foundation and as fully fixed at the base of the foundation. The gravity load was initially applied to generate the initial stresses and water pressure fields. Afterwards, the water head at the cavity was set to 11m in order to initiate water flow in and out the cavity. The alluvium and the dike were considered to be made of the same soil: a mixture of sand and silt. The physical properties and the material parameters, summarized in Table 1 and Table 2, corresponded to the Ottawa 50/200 sand-silt characteristics<sup>36</sup> with  $e_0 = 0.6$ ,  $c_0 = 0.01$  and  $f_{c0} = 0.4$ . The residual fines content was artificially fixed equal to 0.05 for the sake of simplicity in the 3D analysis.

Due to the lack of experimental data, the set of the van Genuchten model parameters used by Uzuoka et al.<sup>28</sup> was adopted, as shown in Table 3. Figure 6 shows the SWCC and the relationship between the relative permeability of water and the degree of water saturation given by the van Genuchten model with the parameters in Table 3.

Table 1 Physical properties of soils

Density of fluid	$\rho_f$	1.0 g/cm <sup>3</sup>	Kinematic viscosity of fluid	$\eta_k$	5.0E-6 m <sup>2</sup> s <sup>-1</sup>
Density of solids	$\rho_s$	2.65	Initial intrinsic permeability	$k$	2.5E-9 m <sup>2</sup>

Table 2 Material constants of soils

Elastic parameters			Plastic parameters			CSL-related parameters				Fines parameters			Erosion parameters
$G_0/MP$	$\nu$	$n$	$k_p$	$A_d$	$\phi_u$	$e_{hc,cr0}$	$e_{fc,cr0}$	$\xi$	$\lambda$	$a$	$m$	$f_{th}$	$\lambda_e$
150	0.2	0.5	0.0017	1	32	0.805	1.03	0.196	0.081	0	0.7	0.3	0.02

Table 3 Material parameters in van Genuchten model

$s_{w,s}$	1.0
$s_{w,r}$	0.1
$\alpha_{vg}$	0.02
$m_{vg}$	0.667
$n_{vg}$	3.0
$\xi_{vg}$	3.5

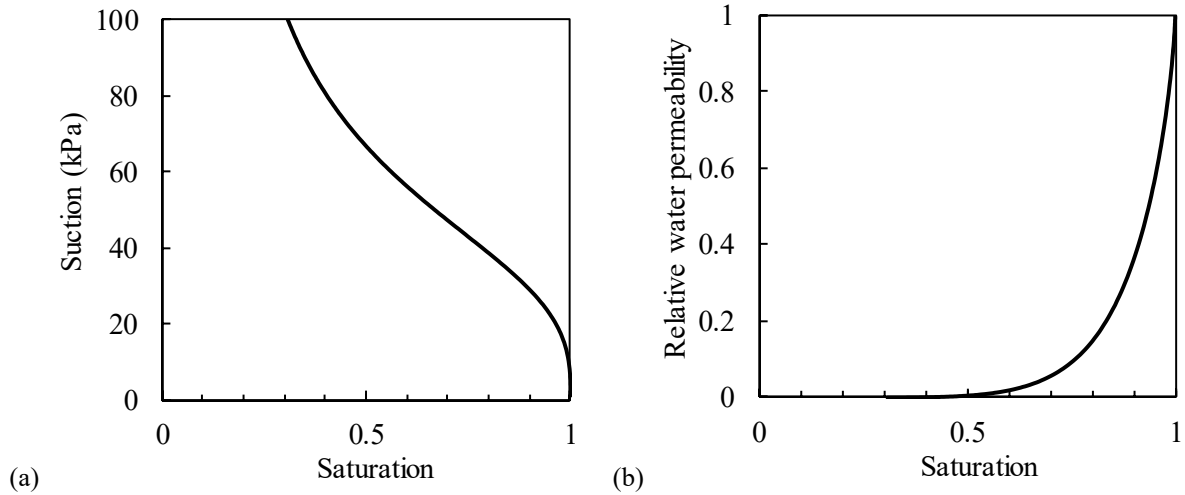


Figure 6 (a) SWCC and (b) relative water permeability using van Genuchten model

However, it should be underestimated that the present work is a theoretical study. The aim is to provide a novel method to identify theoretically the potential consequences of internal erosion developed within a dike under different conditions. The numerical results were analyzed in a qualitative way. With an appropriate erosion law and well calibrated parameters, the numerical results could be compared with the in-situ data in the future. At the present

time, well documented erosion tests and triaxial compression tests with different fines content are still needed. The erosion law and model parameters can be either identified by optimization methods<sup>61-64</sup> or Bayesian based methods<sup>65, 66</sup>.

#### 4.2. Hydro-mechanical responses in 3D condition

Due to the symmetry of the domain and the mechanical and hydraulic boundary conditions, only half the domain was modelled. Figure 7 shows the initial space distribution of the pore pressure in the dike and foundation under the gravity load. The phreatic surface corresponds to the locus of the points at which the pore water pressure is zero. Figure 8 shows the space distribution of the fines content after erosion for Case 1. As internal erosion took place, the fines content which was initially spatially uniform throughout the whole soil volume began to decrease with time. From a numerical point of view, the erosion process is more active where the hydraulic gradient changes more drastically. These analyses in the present paper were theoretical, they were carried out at constant water head and the materials of the dike and the foundation were assumed to be initially homogeneous. The water heads at the upstream and downstream were pre-fixed. The flux was therefore larger along the phreatic surface, especially at the two ends of the phreatic surface. Thus, for this theoretic case, it was reasonable to find a greater loss of fines at the top of the dike and at the bottom of the system along the phreatic surface. The water head may vary slowly or rapidly as a result of rainfall or human intervention. The seepage path and the location of the phreatic surface may become more complex and could evolve with time within a heterogeneous medium. The eroded zone may change accordingly.

Figure 9 and Figure 10 show the displacement and the deviatoric plastic strain fields within the dike at the end of the erosion (time = 30 days) for Case 1. The increase of the void ratio accompanied by a downward shift of the CSL in the  $e-p'$  plane induced by the decrease of the fines content made the soil increasingly looser. Consequently, the soil strength decreased. This led to the onset of a shear sliding surface in the most eroded area near the phreatic surface at the downstream side. The plastic deformation continued to develop with time until the dike ruptured by a sliding of the slope.

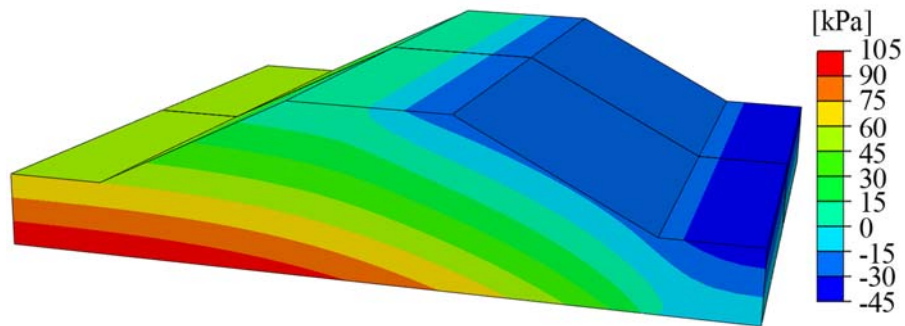


Figure 7 Spatial distribution of initial pore pressure in the dike and foundation under gravity load

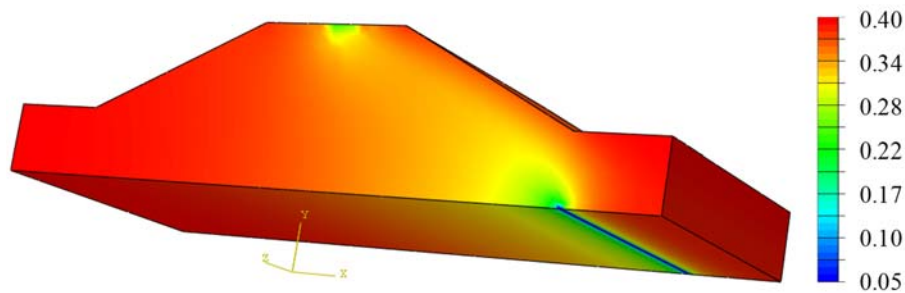


Figure 8 Spatial distribution of fines content after erosion for Case 1 (1/2 model)

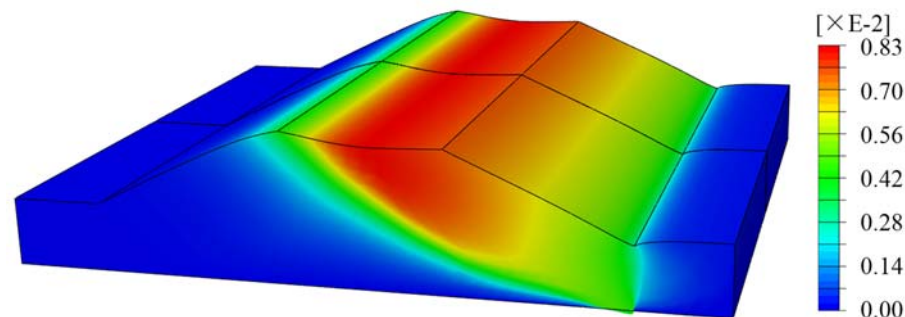


Figure 9 Displacement magnitude field after erosion for Case 1 (Unit: m)

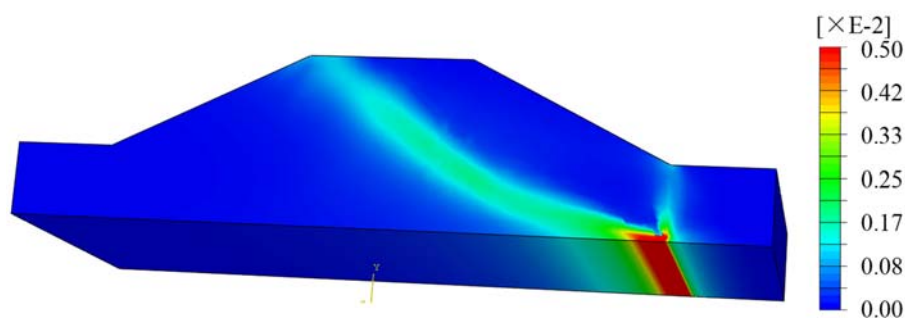


Figure 10 Deviatoric plastic strain field after erosion for Case 1 (1/2 model)

Figure 11 and Figure 12 show the displacement and the deviatoric plastic strain fields within the dike at the end of erosion (time = 30 days) for Case 2 with a leakage cavity of 0.2 m in diameter at the bottom of the symmetry plane. Figure 13 shows the distribution of the fines

content at the end of erosion for Case 2. An area with significant settlement was found at the top of the dike, indicating the inception of a sinkhole as the result of internal erosion. The fine particles close to the leakage cavity were washed out due to high local hydraulic gradients. **The sinkhole was formed due to the volumetric settlements induced by a loosened soil matrix.** It was noted that an eroded zone also developed near the phreatic surface at the downstream side due to the difference in water pressure at the upstream and downstream faces of the dike; this eroded zone led to a global sliding of the dike at the end of the simulation.

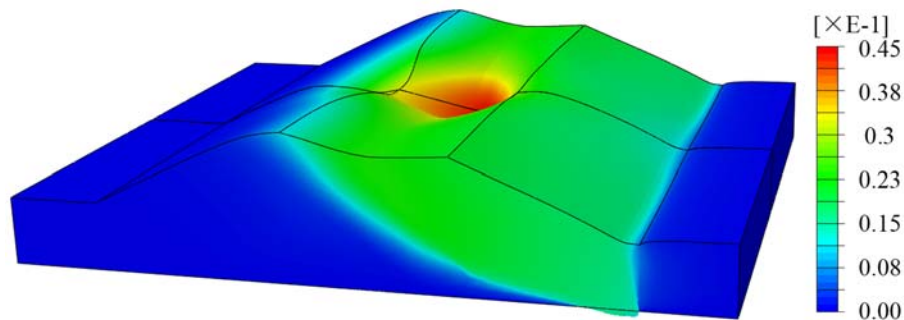


Figure 11 Displacement magnitude field after erosion for Case 2 (Unit: m)

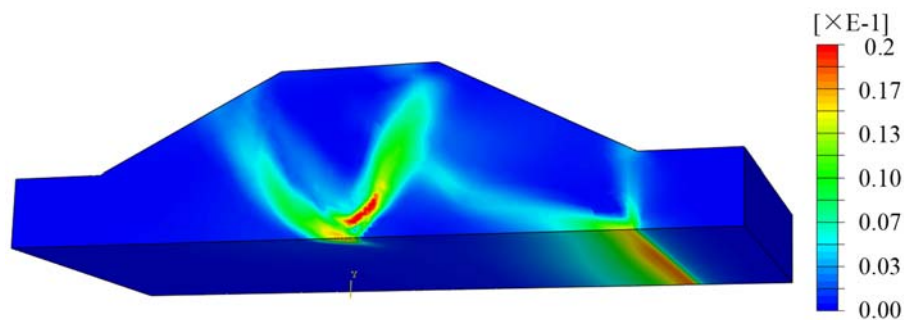


Figure 12 Deviatoric plastic strain field after erosion for Case 2 (1/2 model)

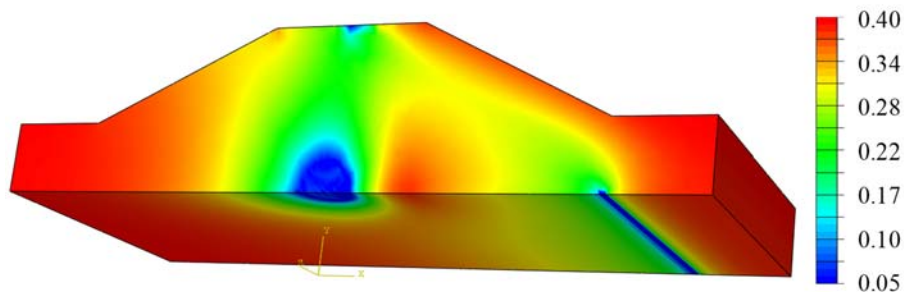


Figure 13 Spatial distribution of fines content after erosion for Case 2 (1/2 model)

**It can be concluded that the shear sliding and the volumetric settlements are two major consequences of the internal erosion. These phenomena depend, to a certain extent, on the**

location of the eroded zones. This aspect, under 2D condition, was discussed in a previous work<sup>29</sup>. In plane strain condition, a significant settlement of the dike was observed when the cavity was located below the top of the dike. In contrast, the results of the 3D simulations showed that the constraint of the surrounding soil limited the development of the deformation, which in turn introduced a local failure (*i.e.* the sinkhole shown in Figure 11-Figure 13) before the global sliding failure occurred.

It should be noted that, in this study, a large value of the erosion parameter  $\lambda_e$  was artificially chosen to reduce the simulation time. However, the time of failure is closely related to the erosion parameters and the permeability of the soil, both of which need to be determined experimentally<sup>17,18</sup> with care.

## 5. Influences of cavity size and water head

### 5.1. Effect of the size of the leakage cavity

In Case 3, a larger leakage cavity of 1.0 m in diameter was established at the bottom of the symmetry plane of the model, as shown in Figure 14, in order to investigate how the size of the leakage cavity influences the development of internal erosion within the dike and foundation.

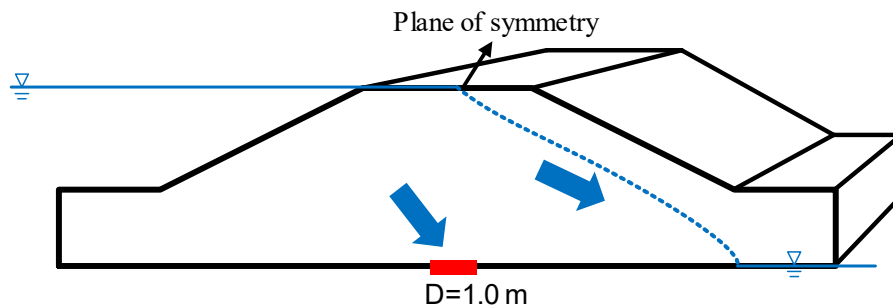


Figure 14 hydraulic boundary conditions for Case 3 with the cavity of leakage (Diameter D=1.0 m)

Figure 15 shows the displacement of the dike-on-foundation at the end of erosion ( $t = 2.5 \times 10^6$  sec) for Case 3. Similar to Case 2, the initiation of a sinkhole as a result of internal erosion was found at the top of the dike. By comparing the time variation of the maximum settlement in Case 2 and Case 3, shown in Figure 16, it is clear that the enlargement of the cavity accelerated the formation of the sinkhole. Figure 17 compares the spatial distribution of the fines content at the end of erosion for Case 2 and Case 3. For a

larger leakage cavity, the internal erosion within the dike and foundation developed faster, leading to the earlier appearance of the sinkhole at the top of the dike.

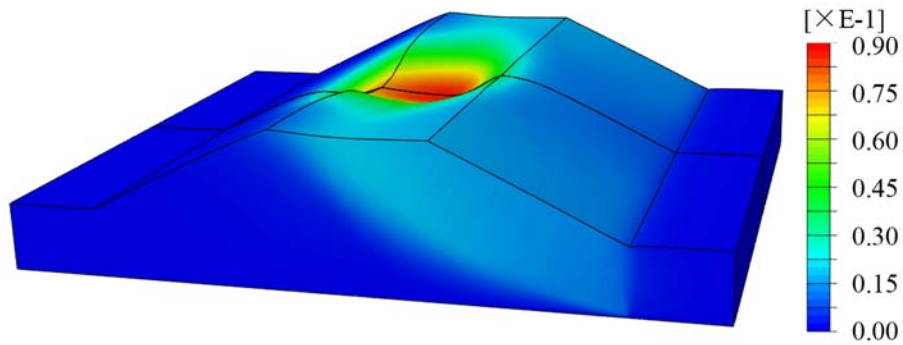


Figure 15 Displacement magnitude field after erosion for Case 3 (Unit: m)

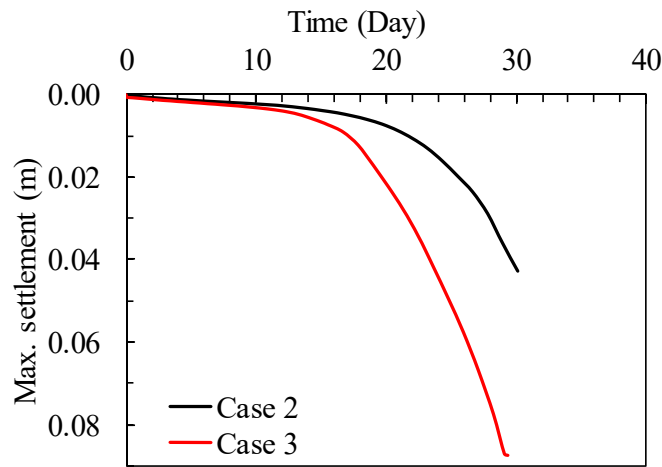
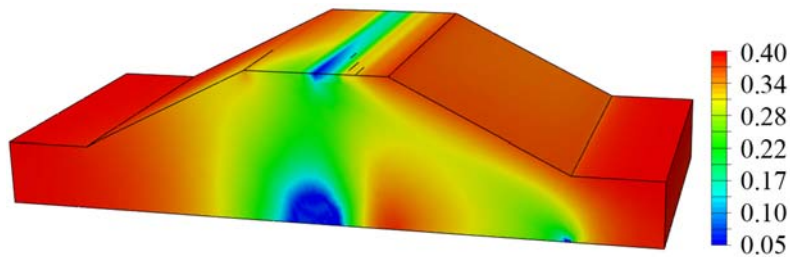
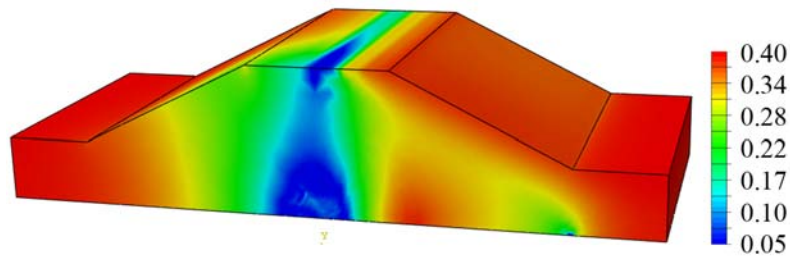


Figure 16 Time variations of the maximum settlement (Point *O* in Figure 3) during erosion for Case 2 and Case 3



(a) Case 2

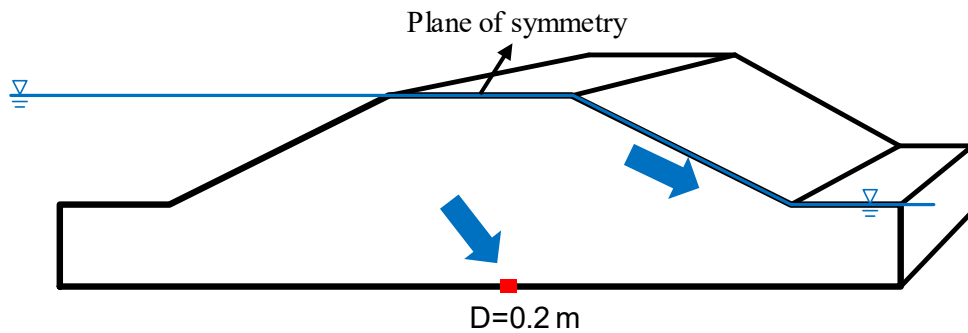


(b) Case 3

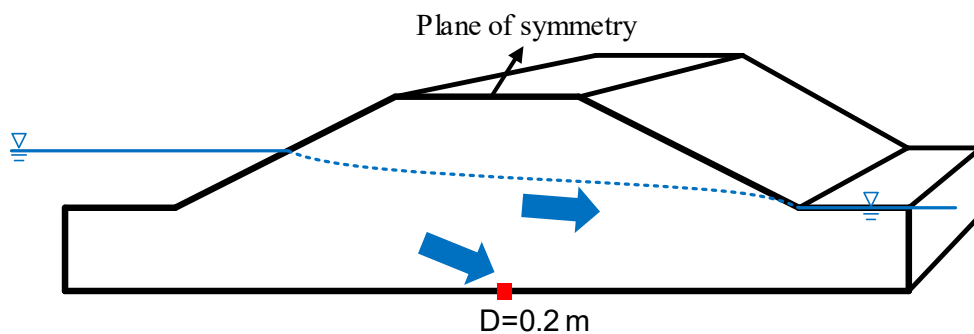
Figure 17 Spatial distribution of fines content after erosion for Case 2 and Case 3 (1/2 model)

### 5.2. Effect of water head

As observed previously, the decrease of the fines content started in the vicinity of the phreatic surface due to the seepage flow induced by the difference in water pressure at the upstream and downstream faces of the dike-on-foundation. Two additional cases were analyzed to investigate how the elevation of the water level upstream and downstream influences the development of internal erosion. In Case 4, the water level at the upstream side was located at the top of the dike, while the water level at the downstream side was supposed to be at the top of the soil foundation. The dike and the foundation were therefore supposed to be saturated as shown in Figure 18(a). In Case 5, the water level at the upstream side was reduced to the middle of the dike height as shown in Figure 18(b).



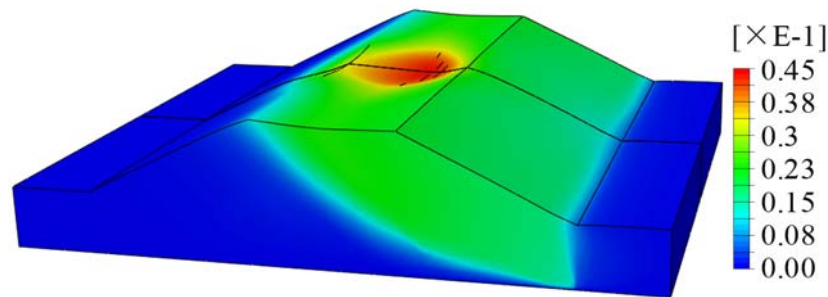
(a) Case 4



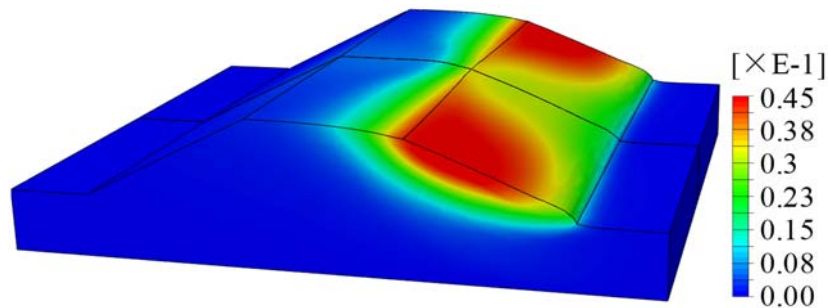
(b) Case 5

Figure 18 Hydraulic boundary conditions for Case 4 and Case 5 with different water levels downstream and upstream

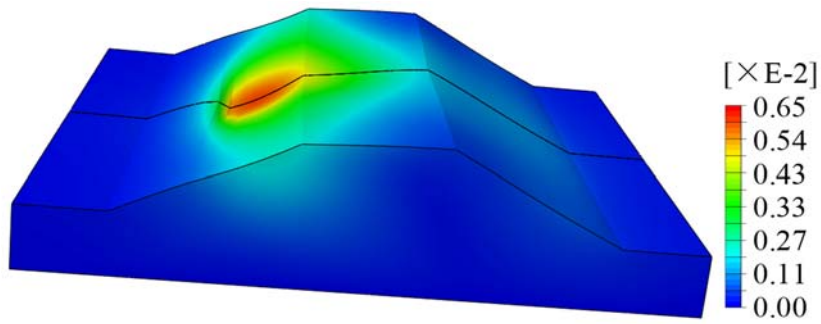
Figure 19 - Figure 21 compare the displacement fields, the deviatoric plastic strain fields and the spatial distributions of the fines content at the end of erosion (time = 30 days) for Case 2, Case 4 and Case 5. In Case 4, a decrease of the fines content at the toe of the dike was observed at the end of erosion, leading to the global sliding failure of the dike at an early stage of erosion. It may be reasonable to assert that the elevation of the water surface within the foundation at the downstream side might have increased the risk of the global sliding failure of the dike. In Case 5, the decrease of the water level at the upstream side of the dike decreased the loss of fines at the toe of the dike. The eroded zone developed by following the direction of the maximum hydraulic gradient. The initiation of a sinkhole was, therefore, found at the upstream side of the phreatic surface. By comparing the results of Case 5 with those of Case 2, it is clear that the location of the sinkhole is to some extent related to the location of the phreatic surface. It should be noted that these analyses were carried out at constant water level. However, in reality, the water level may vary, slowly or rapidly, as a result of rainfall or human activities. More experimental and numerical analyses are still needed in the future to study this aspect.



(a) Case 2

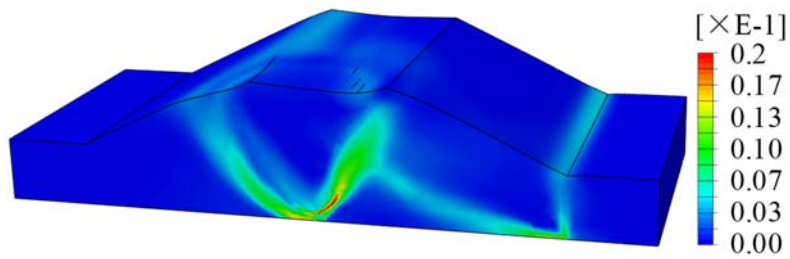


(b) Case 4

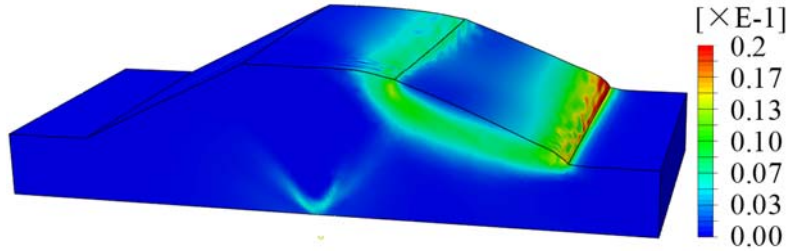


(c) Case 5

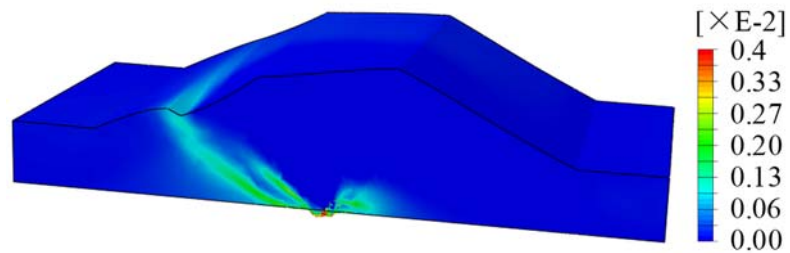
Figure 19 Displacement magnitude field after erosion for Case 2, Case 4 and Case 5 (Unit: m)



(a) Case 2

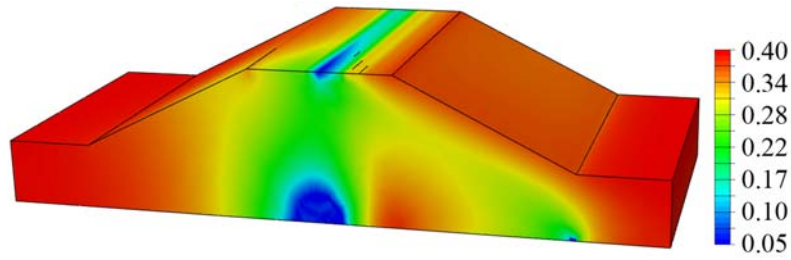


(b) Case 4

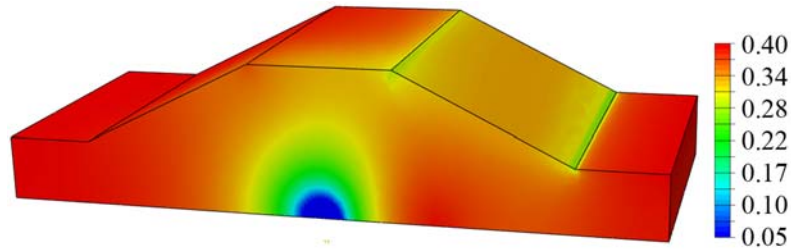


(c) Case 5

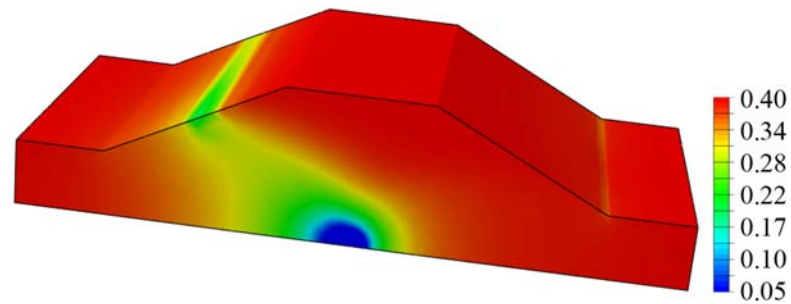
Figure 20 Deviatoric plastic strain field after erosion for Case 2, Case 4 and Case 5 (1/2 model)



(a) Case 2



(b) Case 4



(c) Case 5

Figure 21 Spatial distribution of fines content after erosion for Case 2, Case 4 and Case 5 (1/2 model)

The observations of the Val d'Orléans dike showed that the sinkholes developed at different locations (Figure 22). The formation of these sinkholes was assumed to be due to the presence of karstic cavities below the soil forming the foundation of the dike. It can be seen that the numerical simulations were able to reproduce qualitatively the initiation and the development of these sinkholes whose locations within the dike are strongly related to the seepage conditions.

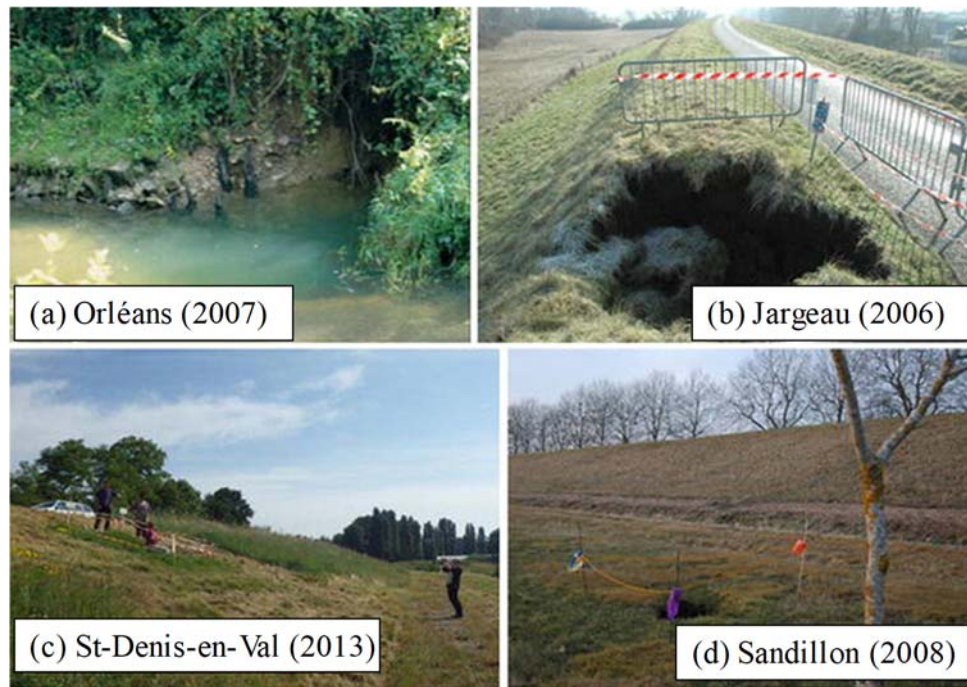


Figure 22 Photos of sinkholes within the Val d'Orléans dike (France) according to Gombert at al.<sup>67</sup>: (a) at the toe of the dike, (b) at the head of the dike, (c) on the slope face of the dike, (d) behind the dike

It can be concluded that the development of internal erosion and the induced deformation of the dike-on-foundation are closely related to its hydraulic boundary conditions. Systematic studies about the influence of the hydraulic boundary conditions (*i.e.* non-constant water head) will surely improve the understanding of the origin of damages or failures induced by internal erosion and serve as a reference to update the specifications for design, construction, and adaptation in order to mitigate and prevent the highest risks.

## 6. Conclusion

This study is an attempt to provide a novel method to identify the potential consequences of internal erosion developed within a dike under different boundary conditions. Even if the analyzed cases were mainly theoretical, they bear a close resemblance to real case problems. The newly developed hydro-mechanical model for internal erosion was enhanced by introducing unsaturated flow in order to describe the seepage within the dike and foundation due to the difference in water pressure at the upstream and downstream sides. This enhanced model was implemented into a 3D finite element code. A stabilized finite element method was used to eliminate spurious numerical oscillations to solve the convection dominated flow of fluidized particles.

Then, a series of 3D simulations of the development of internal erosion within the dike and the foundation were carried out. It was observed that the decrease of the fines content close to the toe of the dike could stimulate a global sliding failure of the slope. The elevation of the water surface within the foundation at the downstream side increased the loss of the fines close to the toe. On the other hand, the presence of a leakage cavity could lead to the initiation of a sinkhole formed as a consequence of the rigid movement of the soil above the eroded area in the vicinity of the cavity. The location of the sinkhole was found to be related to the location of the phreatic surface. Moreover, the enlargement of the cavity accelerated the formation of the sinkhole. For a larger leakage cavity, the internal erosion within the dike and foundation developed faster, leading to the earlier appearance of a sinkhole at the top of the dike. In terms of failure mode, the presence of a leakage cavity introduced a more 'local' failure-collapse mode (*i.e.* a sinkhole) instead of a global sliding failure which was obtained by the numerical simulations performed under plain strain condition. Furthermore, the elevation of the water surface within the foundation at the downstream side increased the risk of a global sliding of the slope.

It is worth mentioning that the erosion model was developed for a saturated medium. In the unsaturated zone, internal erosion is assumed to be negligible due to the absence of seepage forces. However, the development of capillary forces in the unsaturated zone increases the mechanical resistance of the soil. This phenomenon will affect the global mechanical response of the dike. Besides, these analyses were carried out at constant water head and the materials of the dike and the foundation were assumed to be initially homogeneous. In nature, the water head may vary, slowly or rapidly, as a result of rainfall or human activities. The seepage path and the location of the phreatic surface may become more complex and could evolve with time within a heterogeneous medium. The eroded zone may change accordingly. These aspects should be analyzed in future studies.

## **Acknowledgement**

The financial supports provided by a GRF project (Grant No. 15209119) from Research Grants Council (RGC) of Hong Kong and the National Institute for Industrial Environment and Risks of France (INERIS) are gratefully acknowledged.

## Appendix: Brief introduction to the SIMSAND model

Table A1 Basic constitutive equations of SIMSAND

Components	Constitutive equations
Elasticity	$\delta \varepsilon_{ij}^e = \frac{1}{2G} \delta \sigma'_{ij} - \frac{\nu}{2G(1+\nu)} \delta \sigma'_{kk} \delta_{ij}$ $G = G_0 p_{at} \frac{(2.97 - e)^2}{(1+e)} \left( \frac{p'}{p_{at}} \right)^n$
Yield surface in shear	$f_s = \frac{q}{p'} - H$
Potential surface in shear	$\frac{\partial g_s}{\partial p'} = A_d \left( M_{pt} - \frac{q}{p'} \right); \quad \frac{\partial g_s}{\partial s_{ij}} = \{1 \quad 1 \quad 1 \quad 1 \quad 1 \quad 1\}$
Hardening rule for shear	$H = \frac{M_p \varepsilon_d^p}{k_p + \varepsilon_d^p}$
Critical state line and interlocking effect	$e_c = e_{cr0} - \lambda \left( \frac{p'}{p_{at}} \right)^\xi$ $\tan \varphi_p = \left( \frac{e_c}{e} \right) \tan \varphi_\mu \quad \tan \varphi_{pt} = \left( \frac{e}{e_c} \right) \tan \varphi_\mu$

Table A2 Parameters of SIMSAND

Parameters	Definitions
$e_0$	Initial void ratio
$\nu$	Poisson's ratio
$G_0$	Referential shear modulus (dimensionless)
$n$	Elastic constant controlling nonlinear stiffness
$\varphi_\mu$	Critical friction angle
$e_{cr0}$	Reference critical state void ratio
$\lambda$	Constant controlling the slope of CSL
$\xi$	Constant controlling the nonlinearity of CSL
$A_d$	Constant controlling the magnitude of the stress-dilatancy (0.5~1.5)
$k_p$	Plastic modulus (0.01~0.0001)

## References

1. Bonelli S, Marot D. On the modelling of internal soil erosion. In: *The 12th International Conference of International Association for Computer Methods and Advances in Geomechanics (IACMAG)*; 2008.
2. Fell R, Wan CF, Cyganiewicz J, Foster M. Time for development of internal erosion and piping in embankment dams. *Journal of geotechnical and geoenvironmental engineering* 2003, 129:307-314.
3. Wan CF, Fell R. Investigation of rate of erosion of soils in embankment dams. *Journal of geotechnical and geoenvironmental engineering* 2004, 130:373-380.
4. Xu Y, Zhang L. Breaching parameters for earth and rockfill dams. *Journal of Geotechnical and Geoenvironmental Engineering* 2009, 135:1957-1970.
5. Zhang L, Chen Q. Seepage failure mechanism of the Gouhou rockfill dam during reservoir water infiltration. *Soils and Foundations* 2006, 46:557-568.
6. Zhang L, Xu Y, Jia J. Analysis of earth dam failures: A database approach. *Georisk* 2009, 3:184-189.
7. Rönqvist H, Fannin J, Viklander P. On the use of empirical methods for assessment of filters in embankment dams. *Géotechnique Letters* 2014, 4:272-282.
8. Foster M, Fell R, Spannagle M. The statistics of embankment dam failures and accidents. *Canadian Geotechnical Journal* 2000, 37:1000-1024.
9. Muir Wood D. The magic of sands—the 20th Bjerrum Lecture presented in Oslo, 25 November 2005. *Canadian Geotechnical Journal* 2007, 44:1329-1350.
10. Sterpi D. Effects of the erosion and transport of fine particles due to seepage flow. *international journal of Geomechanics* 2003, 3:111-122.
11. Crosta G, Prisco Cd. On slope instability induced by seepage erosion. *Canadian Geotechnical Journal* 1999, 36:1056-1073.
12. Hu W, Hicher P-Y, Scaringi G, Xu Q, Van Asch T, Wang G. Seismic precursor to instability induced by internal erosion in loose granular slopes. *Géotechnique* 2018:1-13.
13. Sibille L, Marot D, Sail Y. A description of internal erosion by suffusion and induced settlements on cohesionless granular matter. *Acta Geotechnica* 2015, 10:735-748.
14. Rochim A, Marot D, Sibille L, Thao Le V. Effects of Hydraulic Loading History on Suffusion Susceptibility of Cohesionless Soils. *Journal of Geotechnical and Geoenvironmental Engineering* 2017, 143:04017025.
15. Moffat R, Fannin RJ, Garner SJ. Spatial and temporal progression of internal erosion in cohesionless soil. *Canadian Geotechnical Journal* 2011, 48:399-412.
16. Chang D, Zhang L. A stress-controlled erosion apparatus for studying internal erosion in soils. *Geotechnical Testing Journal*. 2011, 34:579-589.
17. Marot D, Rochim A, Nguyen H-H, Bendahmane F, Sibille L. Assessing the susceptibility of gap-graded soils to internal erosion: proposition of a new experimental methodology. *Natural Hazards* 2016, 83:365-388.
18. Vardoulakis I, Stavropoulou M, Papanastasiou P. Hydro-mechanical aspects of the sand production problem. *Transport in porous media* 1996, 22:225-244.
19. Stavropoulou M, Papanastasiou P, Vardoulakis I. Coupled wellbore erosion and stability analysis. *International journal for numerical and analytical methods in geomechanics* 1998, 22:749-769.
20. Papamichos E, Vardoulakis I, Tronvoll J, Skjaerstein A. Volumetric sand production model and experiment. *International journal for numerical and analytical methods in geomechanics* 2001, 25:789-808.
21. Cividini A, Gioda G. Finite-element approach to the erosion and transport of fine particles in granular soils. *International Journal of Geomechanics* 2004, 4:191-198.

22. Lominé F, Scholtès L, Sibille L, Poullain P. Modeling of fluid–solid interaction in granular media with coupled lattice Boltzmann/discrete element methods: application to piping erosion. *International Journal for Numerical and Analytical Methods in Geomechanics* 2013, 37:577-596.
23. Mansouri M, El Youssofi MS, Nicot F. Numerical simulation of the quicksand phenomenon by a 3D coupled Discrete Element - Lattice Boltzmann hydromechanical model. *International Journal for Numerical and Analytical Methods in Geomechanics* 2017, 41:338-358.
24. Zhang F, Li M, Peng M, Chen C, Zhang L. Three-dimensional DEM modeling of the stress–strain behavior for the gap-graded soils subjected to internal erosion. *Acta Geotechnica* 2018:1-17.
25. Horikoshi K, Takahashi A. Suffusion-induced change in spatial distribution of fine fractions in embankment subjected to seepage flow. *Soils and Foundations* 2015, 55:1293-1304.
26. van Beek VM, Knoeff H, Sellmeijer H. Observations on the process of backward erosion piping in small-, medium- and full-scale experiments. *European Journal of Environmental and Civil Engineering* 2011, 15:1115-1137.
27. Zhang X, Wong H, Leo C, Bui T, Wang J, Sun W, Huang Z. A thermodynamics-based model on the internal erosion of earth structures. *Geotechnical and Geological Engineering* 2013, 31:479-492.
28. Uzuoka R, Ichiyama T, Mori T, Kazama M. Hydro-mechanical analysis of internal erosion with mass exchange between solid and water. In: *6th International Conference on Scour and Erosion*; 2012.
29. Yang J, Yin ZY, Laouafa F, Hicher PY. Internal erosion in dike - on - foundation modeled by a coupled hydromechanical approach. *International Journal for Numerical and Analytical Methods in Geomechanics* 2019, 43:663-683.
30. Schaufler A, Becker C, Steeb H. Infiltration processes in cohesionless soils. *ZAMM - Journal of Applied Mathematics and Mechanics/Zeitschrift für Angewandte Mathematik und Mechanik* 2013, 93:138-146.
31. Revil A, Cathles L. Permeability of shaly sands. *Water Resources Research* 1999, 35:651-662.
32. Borja RI. On the mechanical energy and effective stress in saturated and unsaturated porous continua. *International Journal of Solids and Structures* 2006, 43:1764-1786.
33. Uzuoka R, Borja RI. Dynamics of unsaturated poroelastic solids at finite strain. *International Journal for Numerical and Analytical Methods in Geomechanics* 2012, 36:1535-1573.
34. Van Genuchten MT. A closed-form equation for predicting the hydraulic conductivity of unsaturated soils. *Soil science society of America journal* 1980, 44:892-898.
35. McKee C, Bumb A. Flow-testing coalbed methane production wells in the presence of water and gas. *SPE formation Evaluation* 1987, 2:599-608.
36. Yin Z-Y, Huang H-W, Hicher P-Y. Elastoplastic modeling of sand–silt mixtures. *Soils and Foundations* 2016, 56:520-532.
37. Jin Y-F, Yin Z-Y, Shen S-L, Hicher P-Y. Investigation into MOGA for identifying parameters of a critical-state-based sand model and parameters correlation by factor analysis. *Acta Geotechnica* 2016, 11:1131-1145.
38. Wu Z-X, Yin Z-Y, Jin Y-F, Geng X-Y. A straightforward procedure of parameters determination for sand: a bridge from critical state based constitutive modelling to finite element analysis. *European Journal of Environmental and Civil Engineering* 2017:1-23.
39. Yin Z-Y, Zhao J, Hicher P-Y. A micromechanics-based model for sand-silt mixtures. *International journal of solids and structures* 2014, 51:1350-1363.

40. Yang J, Yin Z-Y, Laouafa F, Hicher P-Y. Modeling coupled erosion and filtration of fine particles in granular media. *Acta Geotechnica* 2019, 14:1615-1627.
41. Yang J, Yin Z-Y, Laouafa F, Hicher P-Y. Hydro-mechanical modeling of granular soils considering internal erosion. *Canadian Geotechnical Journal* 2019.
42. Yang J, Yin Z-Y, Laouafa F, Hicher P-Y. Analysis of suffusion in cohesionless soils with randomly distributed porosity and fines content. *Computers and Geotechnics* 2019, 111:157-171.
43. Hibbitt, Karlsson, Sorensen. *ABAQUS/standard User's Manual*. Vol. 1: Hibbitt, Karlsson & Sorensen; 2001.
44. Brooks AN, Hughes TJ. Streamline upwind/Petrov-Galerkin formulations for convection dominated flows with particular emphasis on the incompressible Navier-Stokes equations. *Computer methods in applied mechanics and engineering* 1982, 32:199-259.
45. Codina R. Comparison of some finite element methods for solving the diffusion-convection-reaction equation. *Computer Methods in Applied Mechanics and Engineering* 1998, 156:185-210.
46. De Sampaio P. A Petrov–Galerkin/modified operator formulation for convection–diffusion problems. *International Journal for Numerical Methods in Engineering* 1990, 30:331-347.
47. Surana KS, Reddy JN. *The finite element method for boundary value problems: mathematics and computations*: CRC press; 2016.
48. Donea J, Huerta A. *Finite element methods for flow problems*: John Wiley & Sons; 2003.
49. Al-Khoury R. *Computational modeling of shallow geothermal systems*: CRC press; 2011.
50. Zienkiewicz OC, Taylor RL. *The finite element method for solid and structural mechanics*: Elsevier; 2005.
51. Yu CC, Heinrich JC. Petrov - Galerkin methods for the time - dependent convective transport equation. *International journal for numerical methods in engineering* 1986, 23:883-901.
52. Yu CC, Heinrich JC. Petrov—Galerkin method for multidimensional, time - dependent, convective - diffusion equations. *International Journal for numerical methods in engineering* 1987, 24:2201-2215.
53. Dick E. Accurate Petrov - Galerkin methods for transient convective diffusion problems. *International journal for numerical methods in engineering* 1983, 19:1425-1433.
54. Hughes TJR, Mallet M, Akira M. A new finite element formulation for computational fluid dynamics: II. Beyond SUPG. *Computer Methods in Applied Mechanics and Engineering* 1986, 54:341-355.
55. Tezduyar TE, Park YJ. Discontinuity-capturing finite element formulations for nonlinear convection-diffusion-reaction equations. *Computer Methods in Applied Mechanics and Engineering* 1986, 59:307-325.
56. Hughes TJR, Franca LP, Hulbert GM. A new finite element formulation for computational fluid dynamics: VIII. The galerkin/least-squares method for advective-diffusive equations. *Computer Methods in Applied Mechanics and Engineering* 1989, 73:173-189.
57. Codina R, Oñate E, Cervera M. The intrinsic time for the streamline upwind/Petrov-Galerkin formulation using quadratic elements. *Computer Methods in Applied Mechanics and Engineering* 1992, 94:239-262.
58. Al-Khoury R, Bonnier PG. Efficient finite element formulation for geothermal heating systems. Part II: transient. *International Journal for Numerical Methods in Engineering* 2006, 67:725-745.

59. Cui W, Gawecka KA, Potts DM, Taborda DMG, Zdravković L. Numerical analysis of coupled thermo-hydraulic problems in geotechnical engineering. *Geomechanics for Energy and the Environment* 2016, 6:22-34.
60. Alboresha R. Evaluation of the impact of a cavity upon an earth dike (analytical and numerical approaches): Application to the Val d'Orléans area (France). 2016.
61. Jin Y-F, Yin Z-Y, Zhou W-H, Huang H-W. Multi-objective optimization-based updating of predictions during excavation. *Engineering Applications of Artificial Intelligence* 2019, 78:102-123.
62. Yin ZY, Jin YF, Shen JS, Hicher PY. Optimization techniques for identifying soil parameters in geotechnical engineering: comparative study and enhancement. *International Journal for Numerical and Analytical Methods in Geomechanics* 2018, 42:70-94.
63. Yin Z-Y, Jin Y-F, Shen S-L, Huang H-W. An efficient optimization method for identifying parameters of soft structured clay by an enhanced genetic algorithm and elastic–viscoplastic model. *Acta Geotechnica* 2016:1-19.
64. Jin YF, Yin ZY, Shen SL, Hicher PY. Selection of sand models and identification of parameters using an enhanced genetic algorithm. *International Journal for Numerical and Analytical Methods in Geomechanics* 2016, 40:1219-1240.
65. Jin YF, Yin ZY, Zhou WH, Shao JF. Bayesian model selection for sand with generalization ability evaluation. *International Journal for Numerical and Analytical Methods in Geomechanics* 2019.
66. Jin Y-F, Yin Z-Y, Zhou W-H, Horpibulsuk S. Identifying parameters of advanced soil models using an enhanced transitional Markov chain Monte Carlo method. *Acta Geotechnica* 2019, 14:1925-1947.
67. Gombert P, Orsat J, Mathon D, Alboresha R, Al Heib M, Deck O. Role des effondrements karstiques sur les desordres survenus sur les digues de Loire dans le Val D'Orleans (France). *Bulletin of Engineering Geology and the Environment* 2015, 74:125-140.

## Figure captions

Figure 1. Global calculate flow of ABAQUS with the call of UEL subroutine

Figure 2 Scheme of the dike-on-foundation near Orléans (France)

Figure 3 Schematic configuration of the dike and mesh of the numerical model

Figure 4 Mesh of numerical model (1/2 model due to

Figure 5 Boundary hydraulic conditions for: (a) Case1-without the cavity; and (b) Case 2-with the cavity (diameter  $D=0.2$  m)

Figure 6 (a) SWCC and (b) relative water permeability using van Genuchten model

Figure 7 Spatial distribution of initial pore pressure in the dike and foundation under gravity load

Figure 8 Spatial distribution of fines content after erosion for Case 1 (1/2 model)

Figure 9 Displacement magnitude field after erosion for Case 1

Figure 10 Deviatoric plastic strain field after erosion for Case 1 (1/2 model)

Figure 11 Displacement magnitude field after erosion for Case 2 (Unit: m)

Figure 12 Deviatoric plastic strain field after erosion for Case 2 (1/2 model)

Figure 13 Spatial distribution of fines content after erosion for Case 2 (1/2 model)

Figure 14 hydraulic boundary conditions for Case 3 with the cavity of leakage (Diameter  $D=1.0$  m)

Figure 15 Displacement magnitude field after erosion for Case 3

Figure 16 Time variations of the maximum settlement (Point **O** in Figure 3) during erosion for Case 2 and Case 3

Figure 17 Spatial distribution of fines content after erosion for Case 2 and Case 3 (1/2 model)

Figure 18 Hydraulic boundary conditions for Case 4 and Case 5 with different water levels downstream and upstream

Figure 19 Displacement magnitude field after erosion for Case 2, Case 4 and Case 5

Figure 20 Deviatoric plastic strain field after erosion for Case 2, Case 4 and Case 5 (1/2 model)

Figure 21 Spatial distribution of fines content after erosion for Case 2, Case 4 and Case 5 (1/2 model)

Figure 22 Photos of sinkholes within the Val d'Orléans dike (France) according to Gombert at al.<sup>67</sup>: (a) at the toe of the dike, (b) at the head of the dike, (c) on the slope face of the dike, (d) behind the dike